

Characterization of Various IMU Error Sources and the Effect on Navigation Performance

Warren S. Flenniken IV, John H. Wall, David M. Bevly, *Auburn University*

BIOGRAPHIES

Warren S. Flenniken, IV is an M.S. candidate in the Department of Mechanical Engineering at Auburn University. He received a B.S. in Mechanical Engineering in 2000 from Auburn University. He is currently working as a research assistant in the GPS and Vehicle Dynamics Lab in the Department of Mechanical Engineering at Auburn University. His research involves modeling of inertial sensors for use in GPS/INS coupling.

John H. Wall received his B.S. in Mechanical Engineering from Christian Brothers University, and is currently an M.S. candidate in the department of Mechanical Engineering at Auburn University. His research involves the characterization of inertial sensors for the purpose of studying the effects of errors in the computation of navigation solutions.

David Bevly received his B.S. from Texas A&M University in 1995, M.S. from Massachusetts Institute of Technology in 1997, and Ph.D. from Stanford University in 2001 in Mechanical Engineering. He joined the faculty of the Department of Mechanical Engineering at Auburn University in 2001 as an assistant professor. Dr. Bevly is the director of Auburn University's GPS and Vehicle Dynamics Laboratory which focuses on the control and navigation of vehicles using GPS in conjunction with other sensors, such as Inertial Navigation System (INS) sensors.

ABSTRACT

This paper introduces a simple model for modeling inertial sensors and expands on this model to incorporate terms that model the errors associated with high dynamics. The paper uses the techniques of Allan Variance Charts, Monte Carlo Simulations, and Autocorrelation functions to characterize sensors through identification of the error statistics. The error growth of the position and heading navigation solution for two and six degree of freedom scenarios using static error parameters is developed. Analytical expressions for the error growth with wide-band noise are presented and used

as an error baseline for investigating the effects of sensor drift, or walking bias. Experimental data is used to validate the error growth bounds in both scenarios. An advanced sensor model is developed for both an accelerometer and gyro with an explanation of the effects of the dynamic error parameters. A simple rocket trajectory simulation is used to illustrate the adverse effects of high dynamic sensor errors when dead-reckoning with a tactile-grade IMU. Analysis of the advanced model is concluded with an investigation into the relative effect of each error parameter on the trajectory target.

INTRODUCTION

In dead-reckoning navigation scenarios, the integration of noise and bias-corrupted measurements produce large errors in position, velocity, and heading calculations. In order to compensate for the errors and evaluate the effectiveness of the inertial sensors, the chosen accelerometers and rate gyros used must be identified and characterized. A simple model has been developed in [1], which classifies the common errors found in accelerometers and rate gyros into three categories: a constant offset error source, a moving bias error source and a random error source. A procedure has also been developed to obtain the statistics of each of these error sources. When the statistical values for each of the error sources are known, it is possible to use the simple model to statistically simulate an accelerometer's or rate gyro's output.

The raw output of a rate gyro is integrated to obtain a heading estimate. Because the rate gyro measurements have errors, the resultant heading calculation will contain errors as well. Error equations that depict the growth of the error in the heading calculation have been derived in [2]. These error equations were derived with the assumption that the rate gyro has only one error source, wide band noise. The value of this error model is that it may be used to obtain an estimation of the standard deviation of the heading estimate error over time.

More advanced models have been developed that incorporate errors affected by the true accelerations or

rotation rates [3]. These errors include scale factor, misalignment, and nonorthogonality errors.

The primary purpose of this work is to use these existing simple sensor models to identify the common error sources found in accelerometers and rate gyros, and then validate the procedure used to evaluate the statistical properties of each of these error sources. The simple model is then used to classify accelerometers and rate gyros into different grades. Error bounds of some component grades are provided which can be used to determine the utility of a specific grade sensor.

This work also evaluates the effect gravity has on a group of accelerometers and rate gyros when used in an inertial measurement unit. The error growths of the position, velocity and heading calculation are shown when a gravity field is in place, and then the error growths are shown when the gravity field is removed. The comparison reveals the effect a gravity field has on an inertial measurement unit's total error due to the integrity of the gyro measurement.

The final purpose of this work is to identify the effects the error terms in more advanced sensor models have on the position, velocity and heading calculations [3]. A simulated trajectory will be used to evaluate the contribution level each of these errors has on the calculated position, velocity, and heading. The simulated trajectory is designed to be practical and still excite the advance sensor model's error terms.

SIMPLE SENSOR MODEL

The simple model of a gyro assumes that the gyro output (g_r) consists of the true vehicle rotation rate (r) plus a constant offset (c_r), a moving or walking bias (b_r), and wide band sensor noise (w_{gyro}). This model is shown below.

$$g_r = r + c_r + b_r + w_{gyro} \quad (1)$$

The wide band sensor noise (w_{gyro}) is assumed to be normally distributed with a zero mean and sampled covariance [1]

$$E[w_{gyro}^2] = \sigma_{gyro}^2 f_s \quad (2)$$

The moving bias term (b_r), or sensor drift, is modeled as a first order Markov process and is outlined in Equations 2.3 – 2.5. The Markov process takes into account the sampling frequency of the sensor and has the following statistics.

$$E[b_r] = 0 \quad \text{and} \quad E[b_r^2] = \sigma_{gyro\,bias}^2 \quad (3)$$

$$\dot{b}_r = -\frac{1}{\tau_r} b_r + w_{gyro\,bias} \quad (4)$$

Where,

$$w_{gyro\,bias} = \sqrt{\frac{2f_s \sigma_{gyro\,bias}^2}{\tau_r}} v \quad (5)$$

The noise, v , that drives the bias, is normally distributed with zero mean and a sampled covariance of one.

$$v \sim N[0,1] \quad (6)$$

An Allan variance and autocorrelation analysis is used to determine the time constant (τ_r), random walk (σ_{gyro}), and bias variation ($\sigma_{gyro\,bias}$) for the simple model. The numerical values for the various grade sensors are evaluated with an analysis of collected data and verified with the manufacturer's specifications and documents containing published values. This method, once validated can be used for future sensor analysis when exact specifications are unknown.

The simple accelerometer model, similar to the gyro, relates the accelerometer output ($a_{\ddot{x}}$) to the true vehicle acceleration (\ddot{x}), a constant offset or bias ($c_{\ddot{x}}$), a moving or walking bias ($b_{\ddot{x}}$) and a white sensor noise (w_{accel}):

$$a_{\ddot{x}} = \ddot{x} + c_{\ddot{x}} + b_{\ddot{x}} + w_{accel} \quad (7)$$

The accelerometer sensor noise w_{accel} is assumed to be normally distributed with zero mean. The moving bias, or sensor drift, is modeled as a first order Markov process as shown in the gyro model where the noise is also normally distributed with zero mean and the sampled covariance [4].

$$E[w_{accel}^2] = \sigma_{accel}^2 f_s \quad (8)$$

$$E[w_{accel\,bias}^2] = \frac{2f_s \sigma_{accel\,bias}^2}{\tau_{\ddot{x}}} \quad (9)$$

VALIDATION OF INERTIAL SENSOR PARAMETER IDENTIFICATION

It has been shown that Allan variance techniques may be used to identify and verify sensor characteristics [1]. This work uses the simple sensor model and Allan variance charts to verify that simulated sensor models match actual sensor data collected. The simulated sensor, once verified, can be used to determine the error growth of the desired integrated measurement and the

propagation of error in the final navigation solution. Allan variance charts of simulated and experimental KVH-5000 gyro and Humphrey accelerometer data are presented in Figures 1 and 2, respectively.

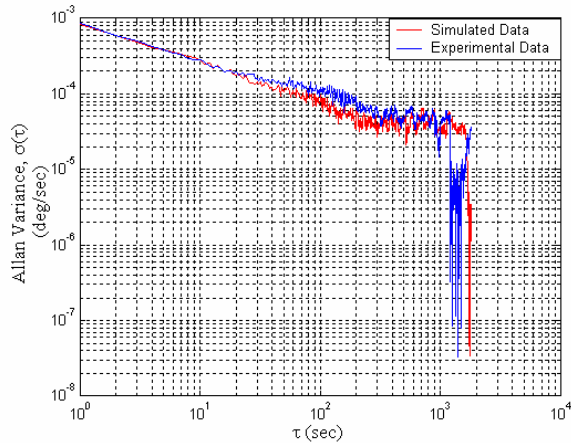


Figure 1.
Allan Variance Comparison II of the KVH 5000
Experimental and Simulated Data

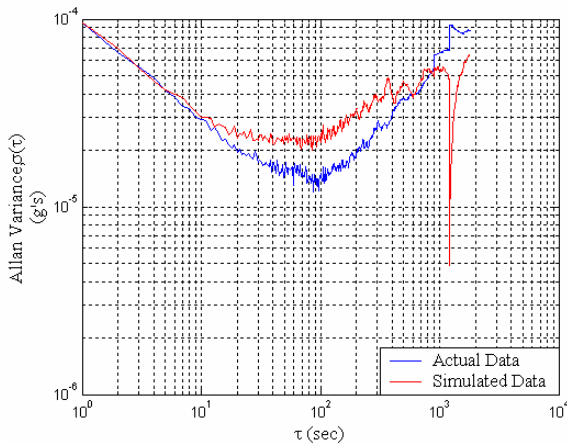


Figure 2.
Allan Variance Comparison of the Humphrey
Accelerometer Experimental and Simulated Data

The close match of the experimental data to the simulated data indicates that the simple sensor model is sufficient to characterize the sensor wide-band noise and walking bias for static tests. Figure 1 shows that the primary error source for the KVH5000 is wide-band noise. The KVH5000 is representative of a sensor with tactile grade specifications. Figure 2 shows that the Humphrey accelerometer sensor is corrupted by both wide-band noise and a walking bias, or sensor drift. The Humphrey accelerometer is representative of a sensor with consumer grade specifications.

INTEGRATION ERRORS DUE TO WALKING BIAS

The effect of walking bias in the sensor measurement is investigated by comparing simulations with and without the moving bias term to an analytical solution for the standard deviation of integrated wide band noise as derived in [2]. This analytical equation will be hereafter referred to as Equation 10.

$$\sigma = \sigma_w T_s \sqrt{k} \quad (10)$$

$$w \sim N[0, \sigma_w] \quad (11)$$

A KVH-5000 gyro was chosen for comparison because its dominate error source is wide-band noise. The results from Monte Carlo simulations produced using the gyro's manufacturer specifications are expected to match the results from the analytical solution with a high degree of confidence. Figure 3 shows the error bounds of the Monte Carlo simulation with moving bias term included. Figure 4 shows the Monte Carlo simulation with moving bias excluded from the sensor model.

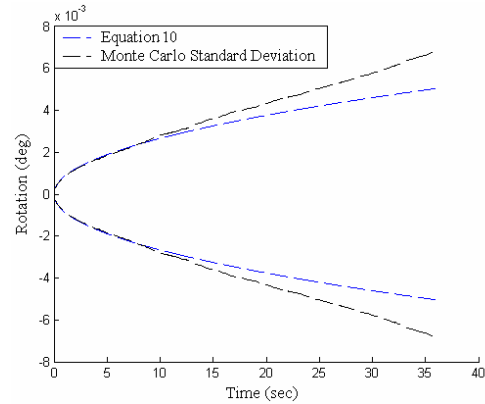


Figure 3. KVH Error Bound Comparison I
Walking Bias Included

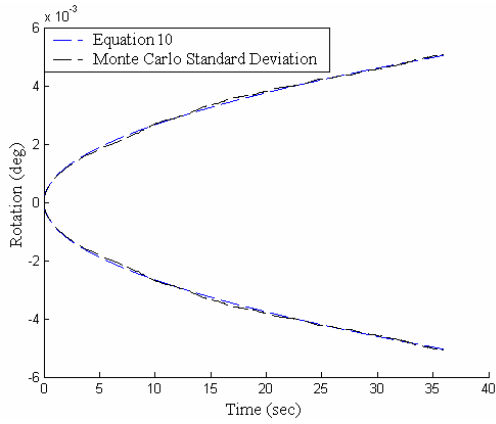


Figure 4. KVH Error Bound Comparison II
Walking Bias Excluded

As expected, the Monte Carlo simulation of the drift-less sensor in Figure 4 matches closely to the analytical solution whereas the sensor model simulation in Figure 3 grows at a faster rate. It is reasonable to assume, therefore, that the bounds derived from the Monte Carlo simulation with both walking bias and wide-band noise adequately represent these error sources. Furthermore, the plot in Figure 5 shows that both the simulated and actual acquired KVH sensor data fall well within the bounds of both the Monte Carlo simulation and analytical equation. The simulated and experimental heading measurement from the KVH sensor, with its tactile grade specifications, falls within the analytical bounds because its primary error source is wide-band noise.

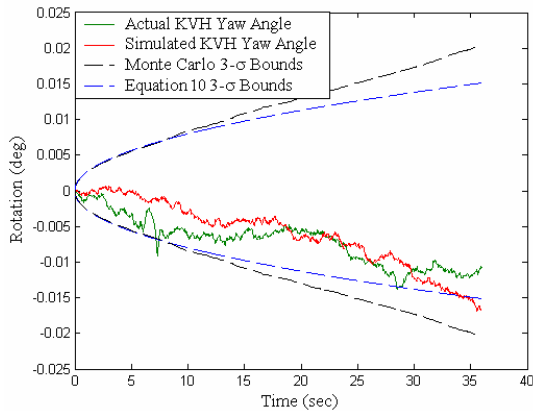


Figure 5. KVH Error Bound Comparison III

DERIVATION OF POSITION AND VELOCITY ERROR GROWTH DUE TO WIDE-BAND NOISE

The following derivation is presented and establishes a baseline for comparison of the effects of bias and noise corrupted measurements in the position and velocity error computation. The derivations for the analytical error

growth of position and velocity errors due to the integration of the sensor model with only wide band noise are performed with a 2DOF IMU model, which includes one accelerometer and one gyro.

The constant bias of the accelerometer is neglected as it is an easily corrected error source. Therefore, the accelerometer measurement becomes:

$$a_{\ddot{x}} = \ddot{x} + w_{accel} \quad (12)$$

Where w_{accel} is the uncorrelated wide band noise of the accelerometer and \ddot{x} is the true acceleration.

Integration of the accelerometer times the heading angle to get longitudinal velocity (V_{North}) results in

$$V_{North} + V_{North}^e = \int (\ddot{x} + w_{accel}) \cos(\psi + \psi^e) dt \quad (13)$$

Assuming the mean acceleration and heading are equal to zero gives

$$\begin{aligned} a &= 0 \\ \psi &= 0 \\ V_{North} &= 0 \end{aligned} \quad (14)$$

Therefore, the longitudinal velocity error (V_{North}^e) is due to the integration of the accelerometer's wide band noise times heading error.

$$V_{North}^e = \int (w_{accel}) \cos(\psi^e) dt \quad (15)$$

A Euler integration of the accelerometer output results in

$$\begin{aligned} V_{North_{k+1}}^e &= V_{North_k}^e + T_s w_{accel_k} \cos(\psi^e) \\ &\approx V_{North_k}^e + T_s w_{accel_k} = \sum_{k=1}^k T_s w_{accel_k} \end{aligned} \quad (16)$$

Squaring and take the expected value of both equations results in

$$E[V_{North}^e (V_{North}^e)^T] = E\left[\left(\sum_{k=1}^k T_s w_{accel_k}\right) \left(\sum_{k=1}^k T_s w_{accel_k}\right)^T\right] \quad (17)$$

Simplifying Equation (17)

$$E[V_{North}^e (V_{North}^e)^T] = T_s^2 \sum_{k=1}^k E[w_{accel_k} (w_{accel_k})^T] \quad (18)$$

Substitute in the covariance of the accelerometer wide band noise to obtain

$$E[V_{North}^e (V_{North}^e)^T] = T_s^2 \sigma_{w_{accel}}^2 k \quad T_s k = t \quad (19)$$

The above equations yield the following approximation for the longitudinal velocity error growth due to the integration of the yaw gyroscopes and accelerometers noises.

$$E[V_{North}^e (V_{North}^e)^T] = T_s t \sigma_{w_{accel}}^2 \quad (20)$$

Finally solving for the standard deviation of the longitudinal velocity results in:

$$\sigma_{V_{North}} = \sigma_{w_{accel}} \sqrt{T_s t} \quad (21)$$

Longitudinal Position Error Equations

The integration of the longitudinal velocity results in the longitudinal position.

$$P_{North} + P_{North}^e = \int (V_{North} + V_{North}^e) dt \quad (22)$$

Assuming the mean longitudinal velocity and position are zero gives:

$$\begin{aligned} P_{North} &= 0 \\ V_{North} &= 0 \end{aligned} \quad (23)$$

Therefore, the longitudinal position error (P_{North}^e) is due to the integration of the longitudinal velocity error (V_{North}^e).

$$P_{North}^e = \int V_{North}^e dt \quad (24)$$

Again, an Euler integration method is used and results in

$$P_{North_{k+1}}^e = P_{North_k}^e + T_s V_{North_k}^e = \sum_{k=1}^k T_s V_{North_k}^e \quad (25)$$

Squaring and take the expected value of both equations results in,

$$E[P_{North}^e (P_{North}^e)^T] = E\left[\left(\sum_{k=1}^k T_s V_{North_k}^e\right)\left(\sum_{k=1}^k T_s V_{North_k}^e\right)^T\right] \quad (26)$$

Simplify to get the following.

$$E[P_{North}^e (P_{North}^e)^T] = T_s^2 \sum_{k=1}^k E[V_{North_k}^e (V_{North_k}^e)^T] = T_s^2 \sum_{k=1}^k \sigma_{V_{North}}^2 k \quad (27)$$

From the above section 3.4 the covariance of the longitudinal velocity was found to be,

$$\sigma_{V_{North}}^2 = T_s^2 \sigma_{w_{accel}}^2 k \quad (28)$$

Therefore, substituting in this for the longitudinal velocity covariance results in the following.

$$\begin{aligned} E[P_{North}^e (P_{North}^e)^T] &= T_s^4 \sigma_{w_{accel}}^2 \sum_{k=1}^k k^2 = \\ &T_s^4 \sigma_{w_{accel}}^2 \left(\frac{1}{3}k^3 + \frac{1}{2}k^2 + \frac{1}{6}k\right) \end{aligned} \quad (29)$$

The above equations result in the following approximation for the longitudinal position error growth due to the integration of the longitudinal velocity error:

$$E[P_{North}^e (P_{North}^e)^T] \approx \frac{1}{3}k^3 T_s^4 \sigma_{w_{accel}}^2 = \frac{1}{3}t^3 T_s \sigma_{w_{accel}}^2 \quad (30)$$

Finally solving for the standard deviation of the northerly position results in:

$$\sigma_{P_{North}} = \sigma_{w_{accel}} \sqrt{\frac{1}{3}T_s t^3} \quad (31)$$

Lateral Velocity Error Equations

As in the longitudinal case the bias of the accelerometer will be assumed to be negligible in the accelerometer measurement. Because of this the following equation is derived:

$$a_{\ddot{x}} = \ddot{x} + w_{accel} \quad (32)$$

where w_{accel} is uncorrelated wide band noise of the accelerometer. Integration of the accelerometer times the heading angle to get lateral velocity (V_{East}) yields

$$V_{East} + V_{East}^e = \int (\ddot{x} + w_{accel}) \sin(\psi + \psi^e) \quad (33)$$

Assuming the mean acceleration and heading are equal to zero gives:

$$\begin{aligned} a &= 0 \\ \psi &= 0 \\ V_{North} &= 0 \end{aligned} \quad (34)$$

Then, the lateral velocity error (V_{East}^e) is due to the integration of the accelerometer's wide band noise time heading error.

$$V_{East}^e = \int (w_{accel}) \sin(\psi^e) \quad (35)$$

An Euler integration of the accelerometer output results in

$$\begin{aligned} V_{East_{k+1}}^e &= V_{East_k}^e + T_s w_{accel_k} \sin(\psi^e) \approx \\ V_{East_k}^e + T_s w_{accel_k} \psi_k^e &= \sum_{k=1}^k T_s w_{accel_k} \psi_k^e \end{aligned} \quad (36)$$

Squaring and take the expected value of both equations results in,

$$E[V_{East}^e (V_{East}^e)^T] = E\left[\left(\sum_{k=1}^k T_s w_{accel_k} \psi_k^e\right)\left(\sum_{k=1}^k T_s w_{accel_k} \psi_k^e\right)^T\right] \quad (37)$$

Knowing that the expected value of the square of the accelerometer noise is simply the covariance of the accelerometer wide-band noise ($\sigma_{w_{accel}}^2$) and that the gyroscope wide-band noise is uncorrelated to the accelerometer wide-band noise the lateral variance can be simplified to the following.

$$E[V_{East}^e (V_{East}^e)^T] = T_s^2 \sum_{k=1}^k E[w_{accel_k} (w_{accel_k})^T] E[\psi_k^e (\psi_k^e)^T] \quad (38)$$

$$E[V_{East}^e (V_{East}^e)^T] = T_s^2 \sum_{k=1}^k \sigma_{w_{accel}}^2 E[\psi_k^e (\psi_k^e)^T] \quad (39)$$

From reference [2] and the above section 3.5:

$$E[\psi_k^e (\psi_k^e)^T] = \sigma_{\vartheta}^2 = T_s^2 k \sigma_{w_{gyro}}^2 \quad (40)$$

Therefore,

$$E[V_{East}^e (V_{East}^e)^T] = T_s^4 \sum_{k=1}^k k \sigma_{w_{accel}}^2 \sigma_{w_{gyro}}^2 \quad (41)$$

$$= T_s^4 \sigma_{w_{accel}}^2 \sigma_{w_{gyro}}^2 \sum_{k=1}^k k = T_s^4 \sigma_{w_{accel}}^2 \sigma_{w_{gyro}}^2 \frac{1}{2} (k^2 + k)$$

$$\approx \frac{1}{2} T_s^4 \sigma_{w_{accel}}^2 \sigma_{w_{gyro}}^2 k^2 \quad T_s k = t \quad (42)$$

The above equations result in the following approximation for the lateral velocity error growth due to the integration of the yaw gyroscopes and accelerometers noises:

$$E[V_{East}^e (V_{East}^e)^T] = \frac{1}{2} T_s^2 t^2 \sigma_{w_{accel}}^2 \sigma_{w_{gyro}}^2 \quad (43)$$

Finally solving for the standard deviation of the lateral velocity results in:

$$\sigma_{V_{East}} = \sigma_{w_{accel}} \sigma_{w_{gyro}} T_s t \sqrt{\frac{1}{2}} \quad (44)$$

Lateral Position Error Equations

The integration of the lateral velocity results in the lateral position.

$$P_{East} + P_{East}^e = \int (V_{East} + V_{East}^e) dt \quad (45)$$

Assuming the mean lateral velocity and position are zero gives:

$$\begin{aligned} P_{East} &= 0 \\ V_{East} &= 0 \end{aligned} \quad (46)$$

So that, the longitudinal position error (P_{East}^e) is due to the integration of the longitudinal velocity error (V_{East}^e), i.e.

$$P_{East}^e = \int V_{East}^e dt \quad (47)$$

Again, an Euler integration method is used and results in,

$$P_{East_{k+1}}^e = P_{East_k}^e + T_s V_{East_k}^e = \sum_{k=1}^k T_s V_{East_k}^e \quad (48)$$

Squaring and take the expected value of both equations results in,

$$E[P_{East}^e (P_{East}^e)^T] = E\left[\left(\sum_{k=1}^k T_s V_{East_k}^e\right) \left(\sum_{k=1}^k T_s V_{East_k}^e\right)^T\right] \quad (49)$$

Simplify the position variance to get the following

$$E[P_{East}^e (P_{East}^e)^T] = T_s^2 \sum_{k=1}^k E[V_{East_k}^e (V_{East_k}^e)^T] = T_s^2 \sum_{k=1}^k \sigma_{V_{East}}^2 k \quad (50)$$

From the above section the covariance of the longitudinal velocity was found to be,

$$\sigma_{V_{East}}^2 \approx T_s^4 \sigma_{w_{accel}}^2 \sigma_{w_{gyro}}^2 \frac{1}{2} k^2 \quad (51)$$

Therefore substituting in this for the longitudinal velocity covariance results in,

$$\begin{aligned} E[P_{East}^e (P_{East}^e)^T] &= \frac{1}{2} T_s^6 \sigma_{w_{accel}}^2 \sigma_{w_{gyro}}^2 \sum_{k=1}^k k^3 \\ &= \frac{1}{2} T_s^6 \sigma_{w_{accel}}^2 \sigma_{w_{gyro}}^2 \left(\frac{1}{4} k^4 + \frac{1}{2} k^3 + \frac{1}{4} k^2\right) \end{aligned} \quad (52)$$

The above equations result in the following approximation for the longitudinal position error growth due to the integration of the longitudinal velocity error:

$$E[P_{East}^e (P_{East}^e)^T] \approx \frac{1}{8} k^4 T_s^6 \sigma_{w_{accel}}^2 \sigma_{w_{gyro}}^2 = \frac{1}{8} t^4 T_s^2 \sigma_{w_{accel}}^2 \sigma_{w_{gyro}}^2 \quad (53)$$

Finally solving for the standard deviation of the northerly position results in:

$$\sigma_{P_{East}} = \sigma_{w_{accel}} \sigma_{w_{gyro}} T_s t^2 \sqrt{\frac{1}{8}} \quad (54)$$

BIAS CONTRIBUTION TO THE IMU INTEGRATION ERROR

Given the derived analytical equations for position and velocity error growth with wide-band noise only, the respective growth effects due the sensor moving bias can be investigated. Figures 6 and 7 show both the simulated and analytical plot of the wide-band noise only error growth as a basis for comparison of the simulation which includes wide band noise and walking bias.

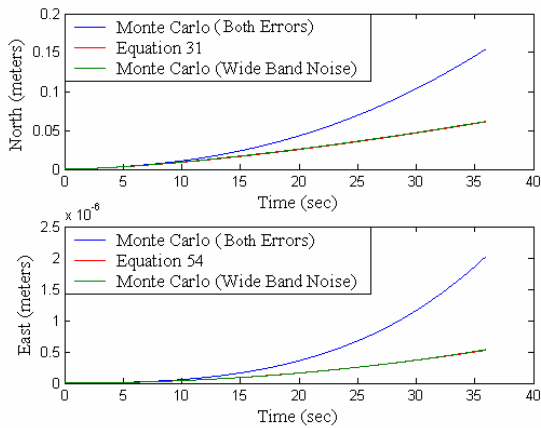


Figure 6. Comparison of a Tactical Grade IMU Position Error Bounds (Static)

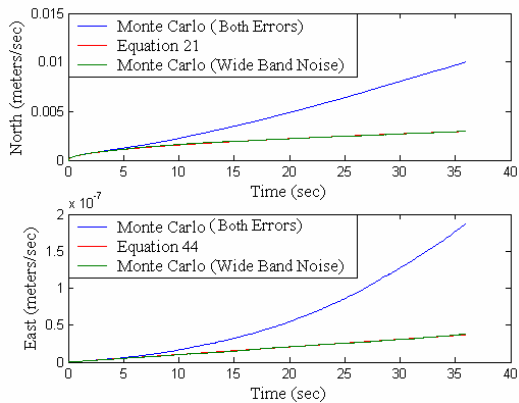


Figure 7. Comparison of a Tactical Grade IMU Velocity Error Bounds (Static)

It is clear from the figures that in both the position and velocity calculations, the errors from the dual error Monte Carlo simulations grow at a significantly higher rate than those of the wide-band noise only case. The sensor moving bias does indeed significantly affect the position and velocity error growth and should be considered as a cogent error source in the inertial sensor model(s) even in the case of a tactical grade IMU.

The 2-DOF IMU simulation is now expanded to a 6-DOF model to simulate a scenario representative of the specific inertial measurement seen in GPS/INS coupling. Monte Carlo simulations of both tactical and consumer grade IMUs are compared. The simulations performed to emulate the sensor include a Markov process modeled moving bias and wide band noise, but excludes the constant bias term. The simulations are run with and without a gravity field to investigate the effects of gravity on the error growth.

Figures 8 and 9 show the growth of the attitude errors due to the integration of tactical and consumer grade IMUs,

respectively. The angles shown are between the body frame and the ENU coordinate frame.

The tactical grade IMU as represented in Figure 8 is dominated by wide-band noise as its shape is congruous to the derived error bounds seen in Figures 3-5. The individual heading errors match well on the plot as they share similar statistics.

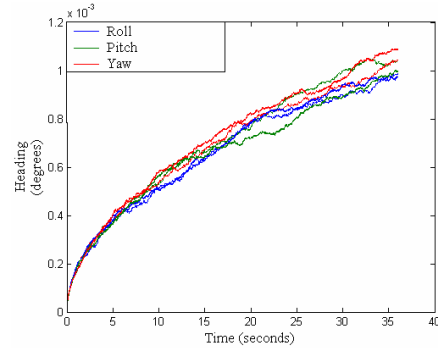


Figure 8. Attitude Error in a Six DoF Tactical Grade IMU

The consumer grade IMU represented in Figure 9 is dominated by wide-band noise in the first few seconds of calculation but eventually appears to grow at a linear rate beyond the initial region. This IMU, seconds after initialization, is soon dominated by sensor walking-bias and grows linearly as is expected from the integration of the moving bias present in the sensor measurement.

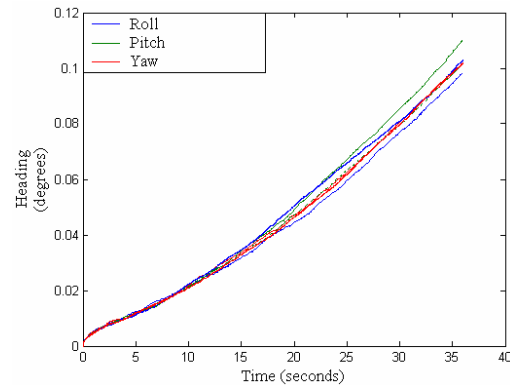


Figure 9. Attitude Error in a Six DoF Consumer Grade IMU

Figures 10 and 11 show simulated position errors as determined by the double integration of the accelerometers for tactical and consumer grade IMUs respectively.

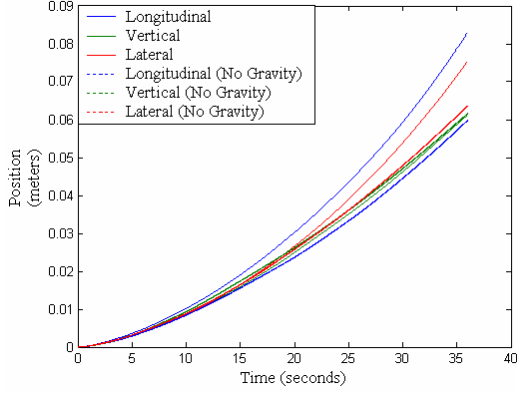


Figure 10. Position Error in a Six DOF Tactical Grade IMU

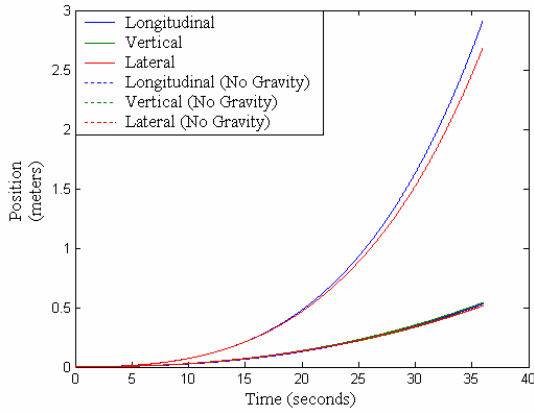


Figure 11. Position Error in a Six DOF Consumer Grade IMU

It is evident that the error for the consumer grade IMU grows much more rapidly than the tactical grade IMU in both plots of attitude and position. Additionally, the consumer grade position error has a more pronounced error growth in the presence of a gravity field than the tactical grade IMU. Because an accelerometer measures specific force, the acceleration due to gravity induces a bias in the sensor and must be subtracted from the measurement when it is oriented in the direction of the gravitational field. Since the orientation of the accelerometer is determined by the IMU gyro measurements, false attitude measurements cause the acceleration calculation to incorrectly include the effects of a gravity field in proportion to the orientation determined by the false gyro measurement. Therefore, the accuracy of the IMU-based attitude (which is significantly worse using the consumer grade gyros) directly impacts the position accuracy obtained from the accelerometers.

ADVANCED SENSOR MODEL

The previous sections have presented an analysis of position and attitude error growth for the static case where the inertial sensors experience no motion. This section presents an advanced sensor model that includes terms that model an inertial sensor's response to motion. The advanced accelerometer model includes the following terms: misalignment, nonorthogonality, scale factor, scale factor asymmetry, and nonlinearity. The advanced terms in the rate gyro model include misalignment, nonorthogonality and scale factor.

The inertial measurement accelerometer triad error model [3], which contains a scale factor error, an asymmetric scale factor error, a nonlinear scale factor error, misalignment errors, nonorthogonality errors and all the non-motion-dependent (static) error terms is given as:

$$a_{\ddot{x}} = (1 + SF_x)\ddot{x} + SFA_x|\ddot{x}| + SFN_x\ddot{x}^2 + \sin(\Delta_{Az} + \delta_{Az})\ddot{y} + \sin(\Delta_{Ay} - \delta_{Ay})\ddot{z} + c_{\ddot{x}} + b_{\ddot{x}} + w_{accel_x} \quad (55)$$

$$a_{\ddot{y}} = (1 + SF_y)\ddot{y} + SFA_y|\ddot{y}| + SFN_y\ddot{y}^2 + \sin(\Delta_{Az} - \delta_{Az})\ddot{x} + \sin(\Delta_{Ax} + \delta_{Ax})\ddot{z} + c_{\ddot{y}} + b_{\ddot{y}} + w_{accel_y} \quad (56)$$

$$a_{\ddot{z}} = (1 + SF_z)\ddot{z} + SFA_z|\ddot{z}| + SFN_z\ddot{z}^2 + \sin(\Delta_{Ay} + \delta_{Ay})\ddot{x} + \sin(\Delta_{Ax} - \delta_{Ax})\ddot{y} + c_{\ddot{z}} + b_{\ddot{z}} + w_{accel_z} \quad (57)$$

Where,

$a_{\ddot{x}}$, $a_{\ddot{y}}$ and $a_{\ddot{z}}$ are the measured accelerations,

\ddot{x} , \ddot{y} and \ddot{z} are the true accelerations,

And,

$|\ddot{x}|$, $|\ddot{y}|$ and $|\ddot{z}|$ are the absolute value of the true accelerations.

The inertial measurement rate gyro triad error model [5], which contains scale factor errors, misalignment errors, nonorthogonality errors and all the error terms as presented in the static case:

$$g_{\phi} = (1 + SF_{\phi})\dot{\phi} + \sin(\Delta_{Gy} + \delta_{Gy})\dot{\vartheta} + \sin(\Delta_{Gz} - \delta_{Gz})\dot{\psi} + c_{\phi} + b_{\phi} + w_{gyro_{\phi}} \quad (58)$$

$$g_{\vartheta} = (1 + SF_{\vartheta})\dot{\vartheta} + \sin(\Delta_{Gy} + \delta_{Gy})\dot{\phi} + \sin(\Delta_{Gx} - \delta_{Gx})\dot{\psi} + c_{\vartheta} + b_{\vartheta} + w_{gyro_{\vartheta}} \quad (59)$$

$$g_{\psi} = (1 + SF_{\psi})\dot{\psi} + \sin(\Delta_{Gz} - \delta_{Gz})\dot{\phi} + \sin(\Delta_{Gx} + \delta_{Gx})\dot{\vartheta} + c_{\psi} + b_{\psi} + w_{gyro_{\psi}} \quad (60)$$

.where,

g_{ϕ} , g_{ϑ} and g_{ψ} are the measured rotation rates,

$\dot{\phi}$, $\dot{\vartheta}$ and $\dot{\psi}$ are the true rotation rates,

and

$|\dot{\phi}|$, $|\dot{\vartheta}|$ and $|\dot{\psi}|$ are the absolute value of the true accelerations.

A list of all of the error terms present in the triad accelerometer model (Equations 55-57) and the triad rate gyro model (Equations 58-60) are given below in Table 1.

Table 1. Advanced IMU Error Parameters

Error Parameter	Symbol	Units
Roll Gyro Constant Offset	c_ϕ	$^\circ/\text{sec}$
Pitch Gyro Constant Offset	c_θ	$^\circ/\text{sec}$
Yaw Gyro Constant Offset	c_ψ	$^\circ/\text{sec}$
Roll Gyro Scale Factor Error	SF_ϕ	ppm
Pitch Gyro Scale Factor Error	SF_θ	ppm
Yaw Gyro Scale Factor Error	SF_ψ	ppm
Gyro Triad Misalignment about X	δ_{G_x}	μrad
Gyro Triad Misalignment about Y	δ_{G_y}	μrad
Gyro Triad Misalignment about Z	δ_{G_z}	μrad
Gyro Triad Nonorthogonality about X	Δ_{G_x}	μrad
Gyro Triad Nonorthogonality about Y	Δ_{G_y}	μrad
Gyro Triad Nonorthogonality about Z	Δ_{G_z}	μrad
Longitudinal Accelerometer Constant Offset	$c_{\ddot{x}}$	g
Vertical Accelerometer Constant Offset	$c_{\ddot{y}}$	g
Lateral Accelerometer Constant Offset	$c_{\ddot{z}}$	g
Longitudinal Accelerometer Scale Factor Error	SF_x	ppm
Vertical Accelerometer Scale Factor Error	SF_y	ppm
Lateral Accelerometer Scale Factor Error	SF_z	ppm
Longitudinal Accelerometer Scale Factor Asymmetry	SFA_x	ppm
Vertical Accelerometer Scale Factor Asymmetry	SFA_y	ppm
Lateral Accelerometer Scale Factor Asymmetry	SFA_z	ppm
Longitudinal Accelerometer Scale Factor Nonlinearity	SFN_x	ppm
Vertical Accelerometer Scale Factor Nonlinearity	SFN_y	ppm
Lateral Accelerometer Scale Factor Nonlinearity	SFN_z	ppm
Accelerometer Triad Misalignment about X	δ_{A_x}	μrad
Accelerometer Triad Misalignment about Y	δ_{A_y}	μrad
Accelerometer Triad Misalignment about Z	δ_{A_z}	μrad
Accelerometer Triad Nonorthogonality about X	Δ_{A_x}	μrad
Accelerometer Triad Nonorthogonality about Y	Δ_{A_y}	μrad
Accelerometer Triad Nonorthogonality about Z	Δ_{A_z}	μrad

MODEL ERROR PARAMETER DESCRIPTIONS

Figure 12 illustrates the individual input/output error types as are present advanced sensor model.

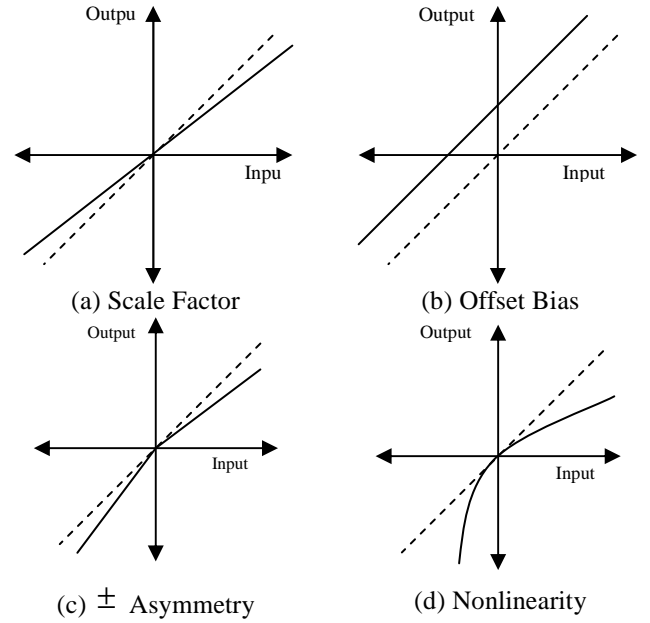


Figure 12. Inertial Measurement Unit Input/Output Error Types

Figure 13 illustrates the individual input axis misalignments. The large arrows in the figure represent the nominal input axis directions (labeled X, Y and Z). The smaller arrows (labeled m_{ij}) represent the directions of scale factor deviations when $i = j$ and axis misalignment when $i \neq j$.

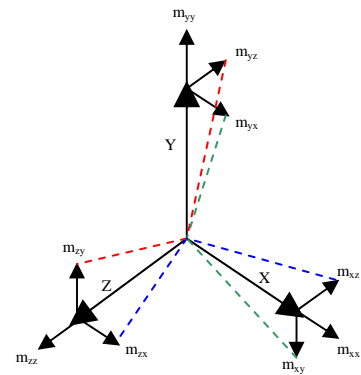


Figure 13. Inertial Measurement Unit Triad Misalignment

The following equations are used to obtain the angular misalignment about a particular axis.

$$\delta_x = \arcsin\left(\frac{m_{yz}}{Y}\right) = \arcsin\left(\frac{m_{zy}}{Z}\right) \quad (61)$$

$$\delta_y = \arcsin\left(\frac{m_{xz}}{X}\right) = \arcsin\left(\frac{m_{zx}}{Z}\right) \quad (62)$$

$$\delta_z = \arcsin\left(\frac{m_{xy}}{X}\right) = \arcsin\left(\frac{m_{yx}}{Y}\right) \quad (63)$$

Figure 14 illustrates the individual input axis nonorthogonality. The large arrows in the figure represent the nominal input axis directions (labeled X, Y and Z). The smaller arrows (labeled m_{ij}) represent the directions of scale factor deviations when $i = j$ and axis nonorthogonality when $i \neq j$.

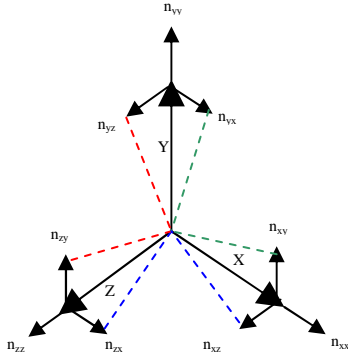


Figure 14. Inertial Measurement Unit Triad Nonorthogonality

The following equations can be used to obtain the angular nonorthogonality about a particular axis.

$$\Delta_x = \arcsin\left(\frac{n_{yz}}{Y}\right) = \arcsin\left(\frac{n_{zy}}{Z}\right) \quad (64)$$

$$\Delta_y = \arcsin\left(\frac{n_{xz}}{X}\right) = \arcsin\left(\frac{n_{zx}}{Z}\right) \quad (65)$$

$$\Delta_z = \arcsin\left(\frac{n_{xy}}{X}\right) = \arcsin\left(\frac{n_{yx}}{Y}\right) \quad (66)$$

INTEGRATION ERRORS OF THE SIX DEGREE OF FREEDOM ADVANCED INERTIAL MEASUREMENT UNIT MODEL

A comparison of the advanced model versus the simple model is illustrated with a common rocket launch trajectory. The comparison identifies the effects of the advanced error parameters by observing the capability of the inertial measurement unit to hit a desired target location.

A simple rocket launch trajectory is simulated to perform the comparison. The rocket is elevated to a pitch angle of 55 degrees before ignition. The longitudinal and lateral axes are aligned with the north and east axis, respectively. A maximum thrust of 8 g's is introduced in the longitudinal direction. The thrust is sufficient to project the rocket a distance of 84 km due north. The body frame

accelerations and heading angles are shown in Figure 15. The rocket velocities in the North-East-Up (NEU) coordinate frame are also shown in Figure 15. A graph of the rockets actual vertical path is shown in Figure 16.

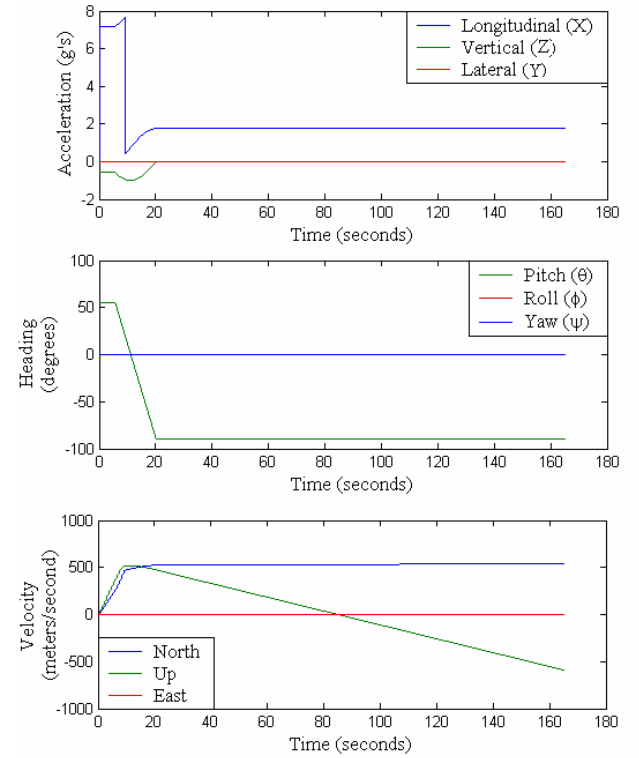


Figure 15. Rocket Launch Trajectory I: Body Accelerations, Body Headings and ENU Velocities

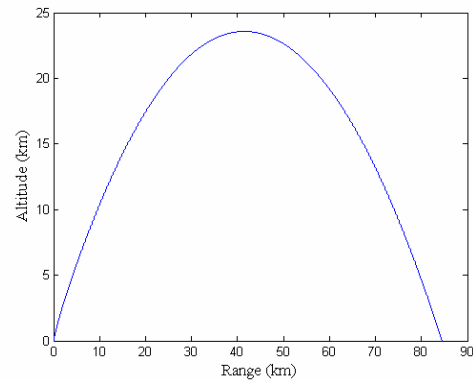


Figure 16. Rocket Launch Trajectory Altitude vs. Range

The simple and advanced six degree of freedom models are run in a Monte Carlo simulation for 200 iterations

using tactical grade IMU specifications. For this comparison, the constant bias offset of the tactical IMU is neglected and the initialization errors are set to zero. The point of comparison is the impact point as shown in Figure 17. The scatter plot of Figure 17 shows the blue scatter with all advanced error terms neglected and the offset red scatter, the result of the Monte Carlo trajectory simulation with both static and advanced error terms included.

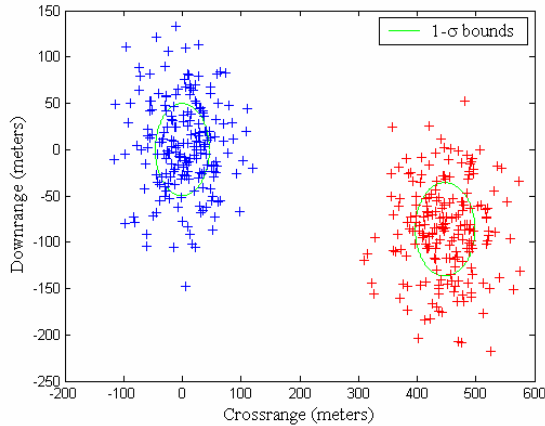


Figure 17. Rocket Launch Trajectory Impact Point Scatter Plot

The standard deviation for both clusters is 50 meters downrange and 50 meters cross range as determined by the resulting 1-sigma bounds. However, from the plot it is evident that the two clusters have significantly different impact means. The mean of the simple model blue scatter has a mean center line at the origin of the downrange and cross range axes as determined by its zero-mean statistics. The advanced red scatter model makes impact with a mean point 450 meters east and 86 meters south of the desired location. Since the moving bias and wide band noise statistics are the same for both models, the shift of the impact point is the sole contribution of the additional input/output parameters in the advanced model. The results of the simulations above exemplify the effects on a navigation solution when using an IMU in high dynamics with uncorrected advanced errors. Note that the advanced model parameters were held constant for each simulated trajectory. In practice with an actual IMU, these values are not necessarily expected to be constant and would lead to a more stochastic final result.

ADVANCED MODEL ERROR PARAMETER CONTRIBUTION LEVELS

For further analysis, the contribution level of each of the advanced error parameters was determined by running the simulated trajectory including only one parameter at a time. The contribution level for each error parameter is

simply the second norm of the error vector at the impact point. Figure 18 is a bar graph depicting the contribution levels resulting from each simulated trajectory.

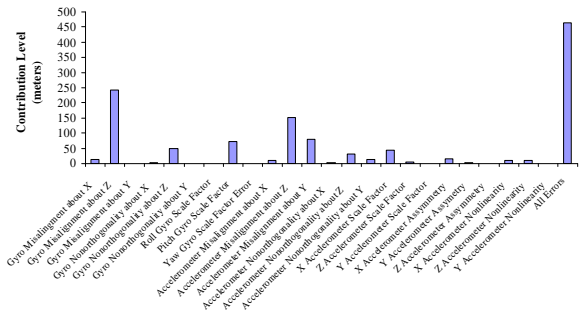


Figure 18. Rocket Launch Trajectory I Error Parameter Contribution Levels

The gyro misalignment about Z has the highest contribution level for the simulated trajectory. This is due to the fact that the yaw measurement is directly affected when there is a pitch rate applied to the body frame, as determined by Equation (60). The accelerometer misalignment about Z is the second highest contributor to the target error. This effect is due to the fact that the downward acceleration is directly affected when there is a longitudinal acceleration applied to the body frame, as modeled by Equation (57). The particular error parameter contribution level distribution (Figure 18) is of course specific to the trajectory simulated and is expected to vary with different trajectory characteristics. It is also important to note that the error parameter contribution levels are not necessarily super-imposable due to the interdependence between error terms.

CONCLUSION

This paper has investigated the propagation of inertial sensor measurement errors into the dead-reckoning or unaided navigation solution. A simple sensor model was developed using the techniques of Allan Variance plots, Monte Carlo simulations, and Autocorrelation functions. Analytical derivations and Monte Carlo simulations were used to compare and depict the various effects of different error sources in the simple model. It was shown that the moving bias or drift of a sensor measurement produces a significant error growth increase in the position, velocity, and heading calculations.

The simple sensor model was used to compare the calculated position error growth for both tactical grade and consumer grade sensors in 2DOF and 6DOF scenarios using manufacturer specifications and Monte Carlo simulations. It was shown that tactical grade inertial sensors significantly outperform consumer grade sensors

though both continuously grow without the aid of referencing information.

The simple sensor model was expanded to include more advanced terms associated with motion. An explanation of the various misalignment, nonorthogonality, scale factor, scale factor asymmetry, and nonlinearity errors are explained in terms of their effect on the direct sensor measurement. A simulated missile trajectory was then used to show the effects of the advanced error sources on an inertial sensor guided rocket. The termination point of the advanced error trajectory was notably corrupted by the errors introduced in the advanced model. The analysis was concluded with an evaluation of the relative contribution of the individual advanced error sources on the final resulting impact point for the given trajectory.

Future work may include a derivation of analytical expressions which describe the error growth contribution due to the walking bias in the position, velocity, and heading calculations. The developed equations can be used in conjunction with the wide-band noise equations to yield a firm quantification of the error growth for a given inertial sensor. With an analytical solution for the position error bounds over time, it would be possible to determine what grade sensor is necessary for a particular application when dead-reckoning or in GPS outages. The analytical equations could provide worse-case estimate of the error growth for a given navigation scenario. Further derivations may include those that analyze the effects gravity has on the error growth in a two degree of freedom scenario and possibly a six degree of freedom scenario. Finally, the advanced model should be further investigated in different environments and high dynamic scenarios similar to the trajectory in this paper. A more in-depth analysis of the contribution levels should be continued as to further document and possibly quantify the effects of the advanced sensor errors for a particular navigation scenario.

ACKNOWLEDGMENTS

This work was partially supported by the U.S. Army Aviation and Missile Research, Development, and Engineering Center (AMRDEC), located at Redstone Arsenal in Huntsville, Alabama.

REFERENCES

- [1] Demoz, Gebre-Eqziabher Design and Performance Analysis of a Low-Cost Aided Dead Reckoning Navigator A Dissertation submitted to the Department of Aeronautics and Astronautics and the committee on graduate studies of Stanford University, Stanford University 2003.
- [2] Bevly, David M. "Evaluation of a Blending Dead Reckoning and Carrier Phase Differential GPS System for Control of an Off-Road Vehicle" 1999 ION/GPS Proceedings
- [3] Grewal, Mohinder S. Global Positioning System, Inertial Navigation and Integration. A John Wiley and Sons, Inc. 2001
- [4] Bennett, S.M. "Fiber Optic Rate gyros as Replacements fro Mechanical Gyros". KVH Industries. 1998.
- [5] Bosch, P. P. J. van den. Modeling Identification and Simulation of Dynamic Systems. CRC Press. 1994.